

# Stimulating Effect of Graphite Admixture on Hydrogen Sorption–Desorption Properties of Mechanically Activated Titanium Powder

C. Borchers,<sup>\*,†</sup> A. V. Leonov,<sup>‡</sup> T. I. Khomenko,<sup>‡</sup> and O. S. Morozova<sup>§</sup>

*Institute of Materials Physics, University of Göttingen, Germany, Chemical Department, Lomonosov Moscow State University, Leninskie Gory, 119899 Moscow, Russia, and Semenov Institute of Chemical Physics RAS, Kosygin St. 4, 119334 Moscow, Russia*

*Received: October 26, 2004*

The effect of graphite admixture on hydrogen sorption–desorption properties of mechanically activated electron microscopy, temperature-programmed reaction, and temperature-programmed desorption techniques. The major effect of graphite addition was found to be the formation of microporous carbon matrix particles containing randomly distributed titanium particles only several nanometers in diameter. This powder architecture enhances hydrogen transport to the titanium surface without hindrances and promotes titanium–hydrogen interaction by modifying the titanium surface and subsurface layers with interstitial carbon atoms.

## 1. Introduction

There is considerable interest in the use of metal hydrides as hydrogen storage media, for reasons of safety, and because metal hydrides have the highest storage capacity by volume. One important drawback is the rather sluggish sorption/desorption rate for most of these hydrides. Therefore, the hydrogen absorbing materials must be activated before use. A number of publications describe different methods designed to ease the activation processes.<sup>1–7</sup> Ball milling of magnesium hydride powder together with various catalysts were studied by Oelerich and co-workers.<sup>3</sup> They compared the catalytic effect of V<sub>2</sub>O<sub>5</sub>, VN, VC, and metallic V on desorption kinetics of MgH<sub>2</sub> and found that the compounds mentioned above considerably enhance hydrogen sorption/desorption, whereas the catalytic effect of pure metals is less pronounced. The mechanism of the catalysis of the compounds is not well understood up to date, but there are some hints that surface effects play a major role.<sup>3,8,9</sup>

Carbon containing compounds and/or graphite were found to be a very promising way to activate hydrogen absorbing metals.<sup>3,9–15</sup> It was found that carbon addition improves the hydrogen absorbing capacity,<sup>14,15</sup> lowers the absorption temperature,<sup>15</sup> passivates the surface of otherwise highly reactive metals,<sup>15</sup> and enhances the hydrogen desorption.<sup>13</sup> Despite a great quantity of investigations done on the activation characteristics of hydrogen adsorbing materials modified by graphite, some important problems have not been clearly solved. The mechanism of this process is poorly understood, as well as the function of the graphite, which seems to be more complicated than described up to now.<sup>12,16</sup> Titanium is chosen as a model system to study metal–hydrogen interaction, as has been done before, see e.g. refs 17 and 18. In this work, we investigate the mechanism of the stimulating effect of graphite addition on hydrogen sorption–desorption properties of mechanically activated titanium powder.

## 2. Experimental Section

Starting powders were elemental titanium with a purity of 99.5% consisting of spherical particles of about 250  $\mu\text{m}$  in diameter and highly oriented pyrolytic graphite powder with a purity of 99.0% and a surface area  $S = 3 \text{ m}^2/\text{g}$ . The milling experiments were carried out under flow conditions in a flow mechanochemical reactor fixed to the vibrator. The following parameters were used for the milling process: A stainless steel container was loaded with 1.8 g of titanium or titanium/graphite reaction mixture consisting of 1.5 g of Ti and 0.3 g of graphite together with 19.8 g of hardened steel balls (diameter 3–5 mm); the vibration frequency was 50 Hz with an amplitude of milling of 7.25 mm; the average energy intensity was 1.0 kW/kg; the flow gas was He with a flow rate of 8–10 mL/min. The milling treatments were carried out at room temperature. After each 1-h run, 2–3 h of sample passivation in helium flow was performed. Only then were the passivated samples taken into ambient atmosphere for further investigations.

The specific surface area  $S$  was measured by the Brunauer–Emmett–Teller (BET) method using low-temperature Ar adsorption.

X-ray diffraction spectra were recorded with a Dron-3 diffractometer with Cu–K $\alpha$  radiation. The phase composition of the samples was determined using JCPDS files provided by the International Center for Diffraction Data. A quantitative X-ray phase analysis was performed using a fitting procedure, where the experimental spectra were approximated with a linear combination of the theoretical spectra of phases and of the background using optimized values of lattice parameters and parameters of broadening of the diffraction maxima of phases. Microstructure and morphology were studied by scanning (SEM) and transmission (TEM) electron microscopy. SEM measurements were carried out using a microprobe Cameca MBX-1M. The TEM investigations were carried out on a Philips EM 420 ST electron microscope with a resolution limit of 0.3 nm and an accelerating voltage of 120 kV. The TEM samples were prepared in an ethanol suspension and placed on copper grids covered by amorphous carbon filaments, which allow the sample particles to stick upon without giving rise to a background of amorphous carbon.

\* Corresponding author e-mail: chris@ump.gwdg.de.

<sup>†</sup> University of Göttingen.

<sup>‡</sup> Lomonosov Moscow State University.

<sup>§</sup> Semenov Institute of Chemical Physics RAS.

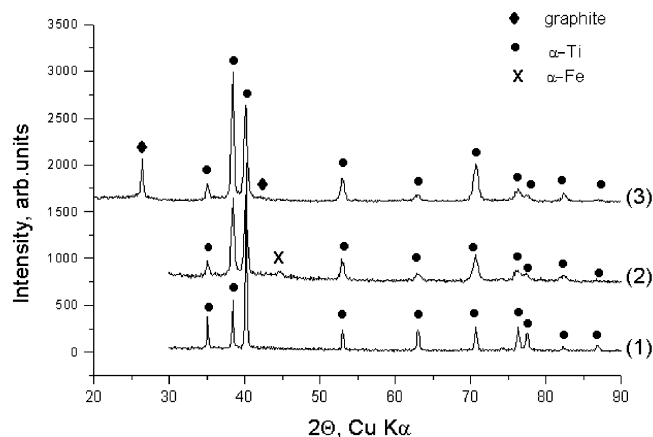


**Figure 1.** XRD patterns of (1) original Ti, (2) pure Ti mechanically activated for 1 h in He flow, and (3) Ti/C mechanically activated for 1 h in He flow.

The hydrogenation and dehydrogenation characteristics were analyzed using temperature-programmed reaction (TPR) and temperature-programmed desorption (TPD) techniques. TPR and TPD measurements were carried out at a heating rate of 10°/min from 20 to 670 °C under flow conditions (flow rate 100 mL/min) using a mixture of Ar – 6 vol %H<sub>2</sub> for sorption and pure Ar for desorption. A quartz flow-reactor was charged with 0.1 g of the testing powder. The testing powder was mixed with 70 wt % of quartz powder in order to minimize the temperature difference between the sample and the surroundings caused by the heat of reaction and to prevent powder caking. The heating was only started when the hydrogen concentration at both the input and the outlet of the reactor was equal. After charging with hydrogen (TPR), the sample was cooled to room temperature during 10–15 min in H<sub>2</sub>/Ar gas flow, which was then changed to pure Ar flow to carry out the TPD experiment. To make TPD, a powder charged with hydrogen in TPR experiment is heated in Ar flow with a heating rate of 10°/min. A heat-conductivity detector was applied to analyze the hydrogen content in the gas phase. The hydrogen portion being adsorbed or desorbed was calculated from the integral intensity of TPR or TPD curve. The effective activation energy of the Ti–H<sub>2</sub> interaction was estimated from an Arrhenius plot constructed from the initial part of each individual TPR curve.<sup>19,20</sup>

### 3. Results

#### 3.1. Mechanical Activation: Structure and Morphology.

Figure 1 shows the XRD patterns of original Ti as well as Ti and Ti/C powders after 60 min of milling. The original powder (1) consists of hcp αTi with  $a = 0.295$  nm,  $c = 0.469$  nm. For the Ti powder milled for 60 min (2), all peaks are broadened, but there is no peak shift as compared to the original Ti powder. There is a strong increase in the relative intensities of the (0002) and (0004) XRD peaks. There are faint αFe peaks, which correspond to ~1.2 wt % of Fe contaminations. No Ti–Fe intermetallic compound can be detected. Curve (3) shows the XRD spectrum of as-milled Ti/C powder containing  $3.2 \times 10^{-2}$  mole Ti +  $2.5 \times 10^{-2}$  mole C. The Ti peak positions are not shifted ( $a = 0.296$  nm,  $c = 0.469$  nm). There are graphite peaks, but no carbide is seen in the spectrum. No iron contamination is detected. Structural parameters of original and as-milled powders are given in Table 1.

The morphologies of original Ti and as-milled Ti and Ti/C powders are shown in the SEM micrographs Figure 2 (A), (B), and (C), respectively. The original Ti powder ( $S = 0.02$  m<sup>2</sup>/g) consists of spherical particles of a narrow size distribution ( $d$

**TABLE 1: Phase Composition of Ti- and Ti/Graphite Powders**

sample	phases	structure	lattice const. [nm]	( <i>S</i> )[m <sup>2</sup> /g]
Ti	αTi	hex	$a = 0.295$ , $c = 0.469$	0.02
Ti milled	αTi	hex	$a = 0.296$ , $c = 0.469$	2.6
Ti/C milled	αFe αTi graphite	hex	$a = 0.296$ , $c = 0.469$	34.6

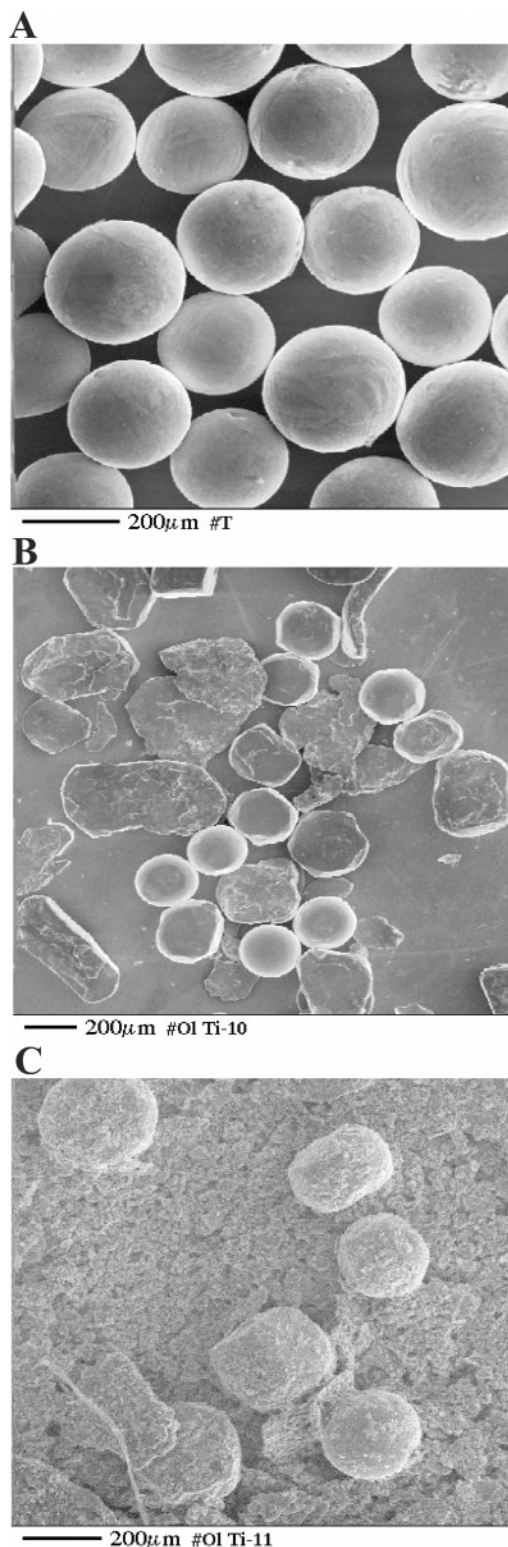
≈ 250 μm). The Ti powder produced during milling consists of a few spherical particles resembling the original ones, deformed particles and flat platelets, the two latter exhibiting a rough surface. The specific surface area of the sample is now considerably larger:  $S = 2.6$  m<sup>2</sup>/g. In contrast, Figure 2(C) shows a drastic change in morphology for the Ti/C powder. The sample is also heterogeneous, but only very few large spherical particles as well as some platelets can be seen. The others are small compared to the as-milled pure Ti: the average particle size is less than 50 μm. The surface of the larger particles appears rough because of small particles placed on the external surface of larger ones. The smallest particles stick together and create 5–10 μm large agglomerations. The specific surface area of this sample is  $S = 34.6$  m<sup>2</sup>/g.

The microstructure of as-milled Ti/C powder was studied by TEM. Figure 3 shows the graphite. In Figure 3(A) the original graphite exhibits rather compact particles with a clear crystalline structure, as can be recognized by the parallel lines in the sword-shaped particle. In Figure 3(B), the graphite after milling can be seen to form ribbonlike structures with a thickness of only a few nanometers, partly crystalline as in the right side of the figure, and partly amorphous as in the left side of the figure. Figure 4 shows Ti-graphite agglomerations. In Figure 4(A), small Ti nanoblocks, about 5 to 15 nm in size, appearing dark, are incorporated into a graphite structure which appears sort of cloudy in the micrograph. The insert in the lower left corner shows a dark-field micrograph of such a structure: Ti particles are now bright spots. It can clearly be seen that the individual Ti nanoblocks are separated from each other by carbon interlayers. Figure 4(B) shows some larger, micron-sized, Ti particles, e.g. in the lower right corner of the micrograph. These particles are also surrounded by carbon layers, appearing cloudy in this micrograph too.

**3.2. Hydrogen Sorption–Desorption Properties.** Temperature-programmed sorption- and desorption techniques, TPR and TPD, were applied to characterize the hydrogen sorption kinetics of the milled powders and the quantity and quality of mechanically created occupation sites available for hydrogen. The structure evolution after TPR and TPD was studied by XRD.

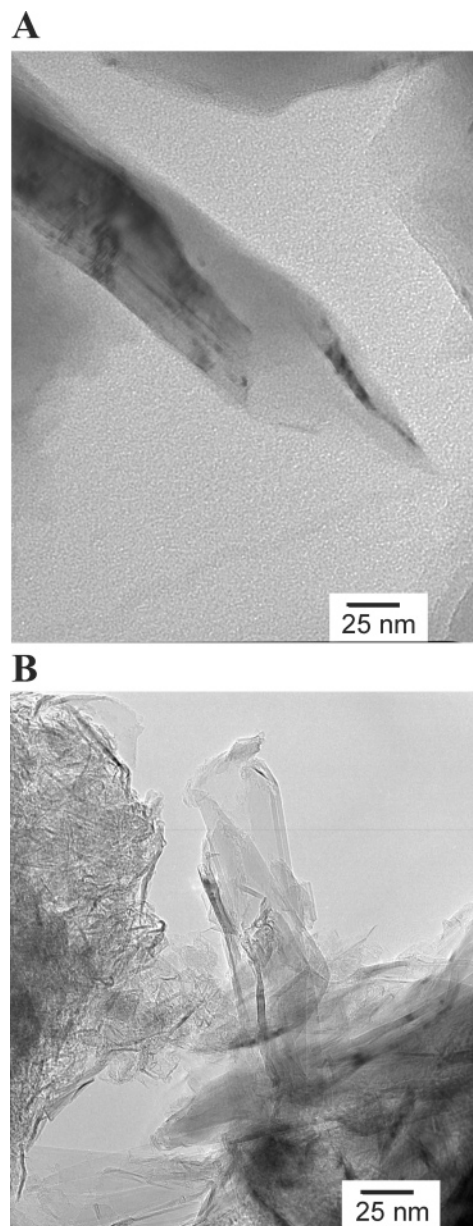
Figure 5(A) shows TPR curves of H<sub>2</sub> with original Ti powder (1), as-milled Ti powder (2), and a TPD curve (3) of milled Ti powder taken after TPR. All three curves exhibit only one single peak. A narrow TPR peak with  $T_{\max} = 659$  °C was observed for the original Ti powder. The effective activation energy of the Ti–H<sub>2</sub> interaction was estimated as 194 kJ/mol. The hydrogen uptake was  $4.5 \times 10^{-4}$  mole H<sub>2</sub>/g Ti, equivalent to H/Ti = 0.5. For the milled powder,  $T_{\max}$  is found to be 566 °C. The effective activation energy can be estimated as 174 kJ/mol. The hydrogen sorption increased to  $7 \times 10^{-3}$  mole H<sub>2</sub>/g Ti, equivalent to H/Ti = 0.7. The TPD spectrum of milled hydrogen-charged Ti powder also exhibits one single peak at about 633 °C. The sample lost  $6.8 \times 10^{-3}$  mole H<sub>2</sub>/g Ti, which is almost the whole initial hydrogen content.

Figure 5(B) shows a TPR curve of H<sub>2</sub> with Ti/C as-milled powders (1), a subsequent TPD curve of this powder (2), and a second TPR carried out after desorption (3). A drastic change



**Figure 2.** SEM micrographs of the morphology of powders after 1 h of milling and corresponding particle size distributions: (A) original Ti, (B) pure Ti as-milled powder, and (C) Ti–graphite as milled powder.

in the TPR spectrum is observed for the milled Ti/C powder, as compared to that of pure Ti powders. The TPR curve exhibits three peaks with  $T_{\max} = 252$  °C, 328 °C, and 423 °C, whereby the mid-peak area  $T_{\max} = 328$  °C occupies only about 6% of the total integral curve intensity. The hydrogen uptakes corresponding to each of the two large peaks were calculated as  $3.8 \times 10^{-3}$  mole  $\text{H}_2/\text{g Ti}$  for  $T_{\max} = 252$  °C and  $12.7 \times 10^{-3}$  mole  $\text{H}_2/\text{g Ti}$  for  $T_{\max} = 423$  °C, corresponding to a final H/Ti ratio



**Figure 3.** TEM micrographs of morphology of (A) original graphite and (B) graphite in Ti/C as-milled powder.

of 1.6. The activation energies of Ti– $\text{H}_2$  interaction were estimated as 37 kJ/mol for  $T_{\max} = 252$  °C and 49 kJ/mol for  $T_{\max} = 423$  °C. TPD exhibits one single peak at  $T_{\max} = 535$  °C with a low-temperature shoulder, corresponding to a loss of  $14.3 \times 10^{-3}$  mole  $\text{H}_2/\text{g Ti}$ , which is 13% less than the total hydrogen uptake. A drastic decrease in hydrogen sorption capacity was observed in the second TPR procedure (3). Only  $1.5 \times 10^{-4}$  mole  $\text{H}_2/\text{g Ti}$  equivalent to  $\text{H/Ti} = 0.014$  was adsorbed at a temperature higher than in the first run,  $T_{\max} = 548$  °C. The parameters of the TPR and TPD processes are listed in Table 2.

To study the structural evolution during TPR and TPD, the phase composition of the powders was determined by XRD after different steps of the TPR and TPD, see Figure 6. Curve (1) in Figure 6(A) shows the original powder after TPR, and curve (2) the milled Ti powder after TPR. Figure 6(B) shows the structural evolution of Ti/C powder in the TPR–TPD–TPR run.

After TPR, the original Ti powder (Figure 6(A) (1)) turned into  $\alpha\text{Ti(H)}$  and 25 wt % of cubic  $\delta\text{TiH}_{1-2}$  (JSPDS 3-859,  $a = 0.440$  nm). The  $\alpha\text{Ti}$  diffraction peaks shifted to  $a = 0.295$  nm



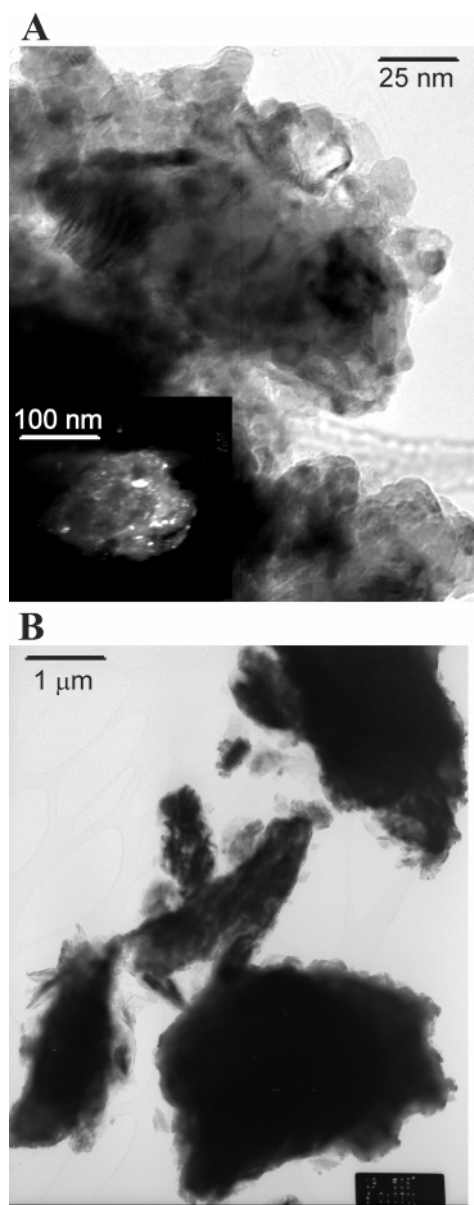


**Figure 4.** TEM bright-field micrograph of (A) composite Ti-graphite particle, Ti nanoblocks sized 5–15 nm in carbon matrix appear dark, inset: dark-field image, Ti nanoblocks appear bright. (B) Ti microblocks surrounded by a carbon shell.

and  $c = 0.472$  nm, indicating a hydrogen dissolution of 2 at. % in  $\alpha$ Ti. Since the hydrogen uptake was up to  $H/Ti = 0.5$  and the amount of  $\delta TiH_{1-2}$  is 25 wt %, the hydride concentration must be near  $\delta TiH_2$ .

The phase composition of the final TPR product for the as-milled Ti powder (Figure 6(A) (2)) is more complicated. Here one finds two hydrogen solid solutions in  $\alpha$ Ti besides two Ti-hydride phases. The compositions of the solid solutions are calculated as Ti-2 at. % H ( $a = 0.295$  nm,  $c = 0.470$  nm) and Ti-8 at. % H ( $a = 0.296$  nm,  $c = 0.475$  nm) from the hydrogen-induced increase of the  $\alpha$ Ti unit cell volume,  $0.28 \text{ nm}^3/\text{H}$ .<sup>21</sup> The Ti-hydride phases were identified as cubic  $\delta TiH_{1-2}$  ( $a = 0.440$  nm), in an amount of 35 wt % and the metastable tetragonal phase  $\gamma TiH_{0.01-0.03}$  (JSPDS 40-1245) with  $a = 0.423$  nm,  $c = 0.449$  nm. Here too, the hydride concentration must be near  $\delta TiH_2$ . As was aforementioned, the sample contains around 1.2 wt % of  $\alpha$ Fe. After TPD (not shown, see ref 26), the sample still contains  $\alpha$ Ti and a small amount of the metastable  $\gamma TiH_{0.01-0.03}$ , while  $\delta TiH_{1-2}$  has dissolved.

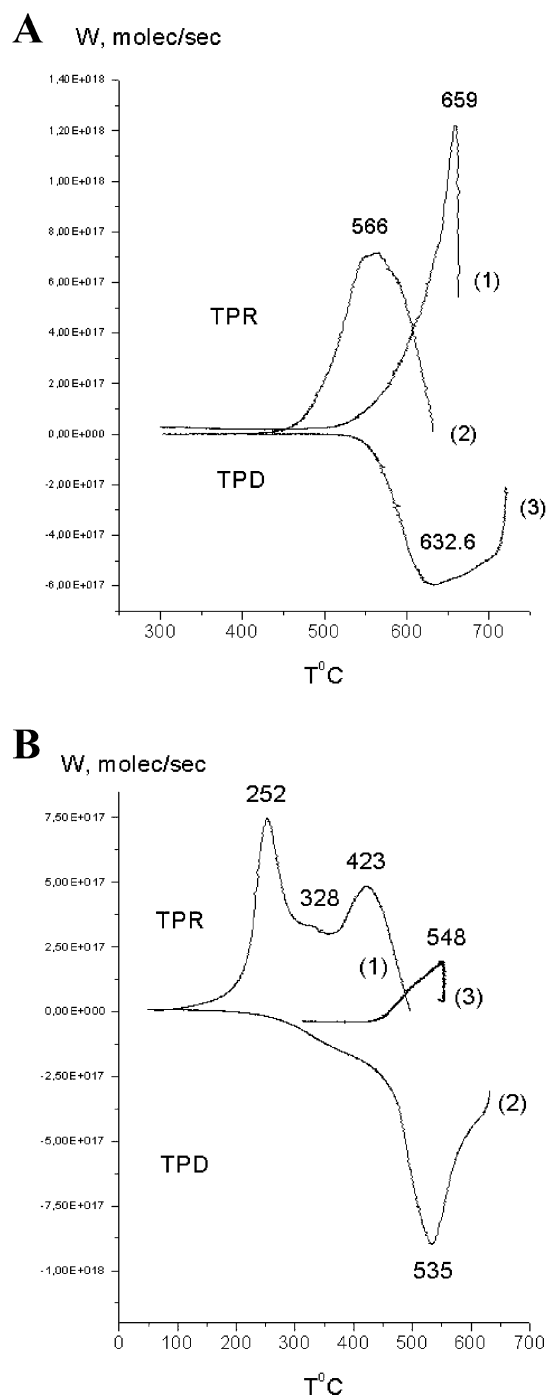


**Figure 5.** TPR and TPD curves for (a) pure Ti powders: (1) TPR for original Ti; (2) TPR for as-milled Ti powder; (3) TPD for as-milled Ti powder, and for (b) Ti/C as-milled powder: (1) TPR; (2) TPD; (3) second TPR after desorption.

**TABLE 2: Parameters of TPR and TPD Processes**

sample		$T_{\max}$ [°C]	$E_A$ [kJ/mol]	H-uptake [H/Ti]		$T_{\max}$ [°C]	$E_D$ [kJ/mol]	H-loss
Ti orig.	TPR	658	194	0.5				
Ti mill.	TPR	566	174	0.7	TPD	633	188	97%
Ti/C	TPR	253	37	0.4	TPD			
milled		328				368		
		423	49	1.2		535	168	87%
Ti/C	TPR	548		0.014				
milled	2. run							

In the case of the mechanically activated Ti/C powder, the phase transformation was tested after each TPR peak and after desorption, see Figure 6(B). In the XRD pattern recorded after

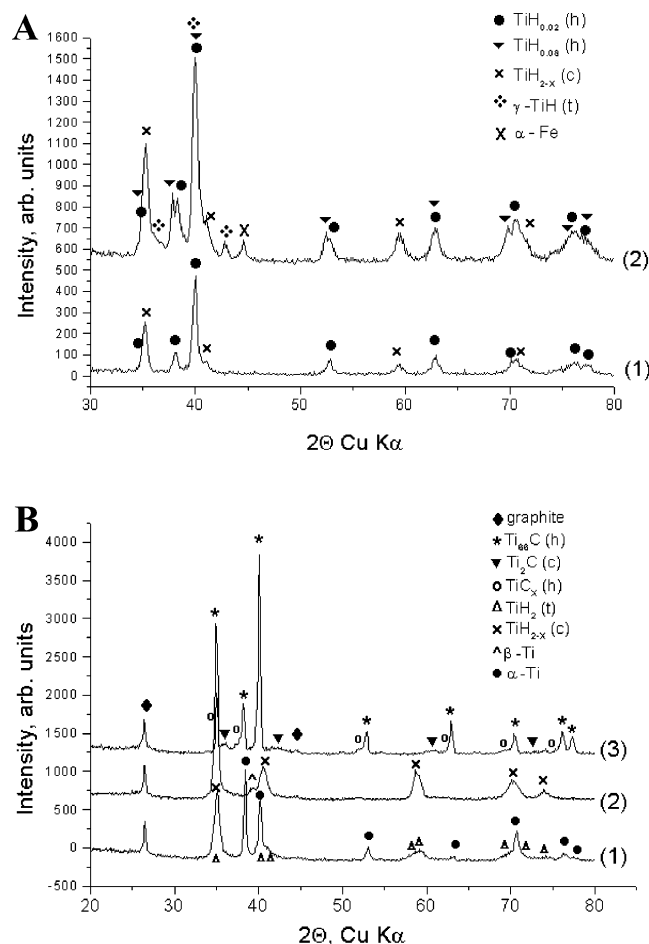


**Figure 6.** XRD patterns for TPR and TPD experiments shown in a. XRD patterns of pure Ti samples (A) after TPR: (1) original Ti; (2) as-milled Ti powder, and (3) after TPD. (B) XRD patterns for TPR and TPD experiments shown in b. XRD patterns of pure Ti/C as-milled powder (1) after the first TPR peak, (2) after the second TPR peak, and (3) after TPD.

the first TPR peak (curve 1), graphite and  $\alpha\text{Ti}$  ( $a = 0.294$  nm,  $c = 0.467$  nm) are detected, besides broad peaks attributed to the tetragonal hydride  $\epsilon\text{TiH}_2$  with  $a = 0.315$  nm,  $c = 0.437$  nm (JSPDS 9–371), existing to an amount of about 25 wt %. No diffraction peaks of  $\alpha\text{Ti}$  are observed in the XRD pattern of the final TPR product (curve 2). The peaks are attributed to the cubic phase  $\delta\text{TiH}_2$  with  $a = 0.444$  nm and a small amount of  $\beta\text{Ti}$ –40 at. % H with  $a = 0.330$  nm.

No hydrides are detected by XRD pattern after TPD, see Figure 6(B), curve 3. Instead, carbides are observed. The final TPD product consists of two solid solutions in  $\alpha\text{Ti}$ ,  $a = 0.296$  nm,  $c = 0.471$  nm and  $a = 0.297$  nm,  $c = 0.478$  nm, and the cubic  $\text{Ti}_2\text{C}$  ( $a = 0.859$  nm) besides graphite. Phase compositions and structural parameters of original and as-milled powders after TPR and TPD are given in Table 3.

#### 4. Discussion

A close examination of the experimental data shows that ball-milling as well as graphite addition and milling significantly improve the reactivity of titanium toward hydrogen by modifying some characteristics of the original powder. While the missing Fe peaks in the Ti/C powders are due to wet operation in the presence of graphite, the Fe peaks observed in pure Ti powders are due to dry operation with stainless steel balls. Even after heating under TPR, no Ti–Fe intermetallic phases are observed, so a possible stimulating effect of Fe on hydrogen

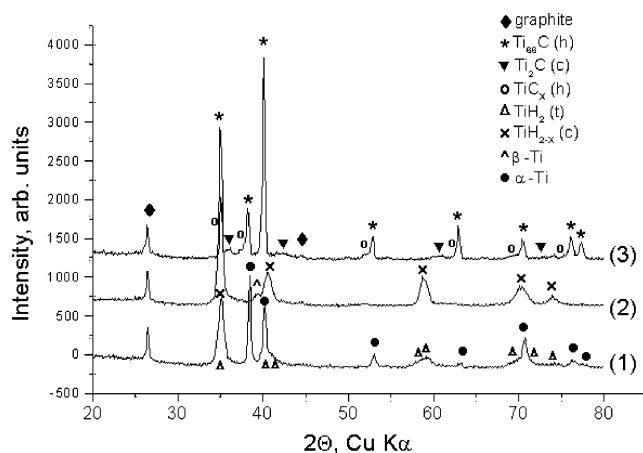


**Figure 7.**

**TABLE 3: Phase Composition of Ti- and Ti/Graphite Powders after TPR/TPD**

sample	treatment	phases	structure	lattice constants [nm]
Ti	TPR	$\alpha\text{Ti}$ –2 at. % H	hex	$a = 0.296$ , $c = 0.472$
	original	$\delta\text{TiH}_{1-2}$	cub	$a = 0.440$
Ti	TPR	$\alpha\text{Ti}$ –2 at. % H	hex	$a = 0.295$ , $c = 0.470$
		$\alpha\text{Ti}$ –8 at. % H	hex	$a = 0.296$ , $c = 0.475$
		$\delta\text{TiH}_{1-2}$	cub	$a = 0.440$
		$\gamma\text{TiH}_{0.01-0.03}$	tet	$a = 0.423$ , $c = 0.449$
	TPD	$\alpha\text{Ti}$ –2 at. % H	hex	$a = 0.295$ , $c = 0.470$
		$\gamma\text{TiH}_{0.01-0.03}$	tet	$a = 0.422$ , $c = 0.452$
		$\alpha\text{Fe}$		
Ti/C	TPR 1.peak	$\alpha\text{Ti}$	hex	$a = 0.296$ , $c = 0.468$
		$\epsilon\text{TiH}_2$	tet	$a = 0.315$ , $c = 0.437$
	TPR 2.peak TPD	graphite		
		$\delta\text{TiH}_{1-2}$	cub	$a = 0.444$
		$\alpha\text{Ti(H)}$	hex	$a = 0.296$ , $c = 0.471$
		$\alpha\text{Ti(C)}$	hex	$a = 0.297$ , $c = 0.478$
		$\text{Ti}_2\text{C}$	cub	$a = 0.859$

sorption–desorption properties are taken to be negligible, particularly since Fe has, contrary to Ti, a positive heat of mixing with H.

**4.1. Pure Ti Powder.** Under ball-milling, Ti powder attains a flakelike and fragmented morphology, with a substantially higher specific surface area  $S$  than the original powder. During this milling, flakes with a (0001) habit plane are formed, as reflected in the intensity shift of XRD peaks. Together with this, a high defect concentration is introduced into the powder, as reflected by the high specific surface area  $S$ , indicating on a large number of internal sites accessible for Ar adsorption during BET measurements. Consequently, the hydrogen sorption properties are modified, as compared to the original powder, see Figure 5(A). While the original powder exhibits a sharp peak at  $T_{\text{max}} = 659$  °C, the peak position of the milled powder has fallen to  $T_{\text{max}} = 566$  °C. The peak has broadened, and the activation energy for hydrogen uptake has decreased by 20 kJ/mol. Moreover, the hydrogen sorption and conversion of Ti to Ti hydride is found to be about 1.4 times larger for the as-milled sample, as for the original powder.

According to common opinion, hydrogen atoms randomly occupy tetrahedral interstitial sites having the same energy in the undisturbed bcc  $\alpha\text{Ti}$  lattice. However, as was shown for hydrogen-disordered or amorphous alloys and for hydrogen-interstitial solid solutions,<sup>19,22–24</sup> there may be different types of sites with a different coordination number of metal atoms or a different number of interstitial atoms located in neighboring octahedral sites. Such a distribution in chemical as well as in geometrical configuration leads to a distribution of site energies

for H atoms. If the variation in local environments around positions available for hydrogen is randomly and continuously distributed in the bulk, a continuous type of site-energy distribution is realized. This type of distribution manifests itself in broadening of the TPR (or TPD) peaks. As shown by Bouaricha and co-workers,<sup>12</sup> the gas–solid reactivity increases with decreasing crystallite size of the solid. The fragmented and highly disturbed powder morphology seems to decrease the diffusion hindrances usual for gas–solid reactions. Ti-hydride formation is a diffusion and interface velocity controlled reaction.<sup>25</sup> The process goes through several stages. The first is dissociative adsorption of hydrogen at the surface, followed by diffusion of hydrogen atoms into the bulk. Due to the particle size reduction, the amount of near-surface states is higher in the milled powders as compared to the original ones, leading to a decrease in  $T_{\max}$  and activation energy. Furthermore, lattice defects which are present in very high concentrations and are accessible even for large Ar atoms lead to an enhanced diffusion and intensify these effects.

After desorption of H, the milled Ti powders contain a small amount of residual  $\alpha$ Ti–H solid solution as well as the metastable  $\gamma$ TiH<sub>0.01–0.03</sub>, whereas the hydride phases are dissolved. The desorption peak is 70° higher than the sorption peak, but it is also quite broad. In a previous work, the desorption properties of pure and milled commercial TiH<sub>2</sub> were studied.<sup>26</sup> Pure TiH<sub>2</sub> exhibits one sharp desorption peak with  $T_{\max} = 541$  °C, while milled TiH<sub>2</sub> has a quite broad peak with  $T_{\max} = 519$  °C.<sup>26</sup> This was also explained by high defect concentrations after milling, in good agreement with the findings in this work.

**4.2. Ti/C Powder.** A remarkable change in the structural properties of Ti powder is observed after carbon addition and ball-milling. Graphite addition greatly enhances the powder fragmentation, as can be seen in Figure 2. Whereas milling of the pure metal leads mainly to flattened but basically whole powder particles, nanoparticles suspended in a carbon matrix are formed after milling in the presence of graphite. As a result,  $T_{\max}$  falls down to 253 °C–423 °C. The hydrogen sorption increases more than 3 times as compared to the original powder. However, these changes cannot be attributed only to the particle size reduction.

Another important role of graphite is that of an anti-sticking and matrix-forming agent. TEM micrographs show that a 1-h milling treatment is sufficient to disrupt the regular structure of graphite and to create porous and partly amorphous material (see Figure 3). These porous graphite structures serve as a matrix for the Ti nanoparticles, preventing their sticking to one another, and as an enveloping agent for Ti microparticles. No carbon-free metal surface is observed after common milling of Ti and graphite. It should be mentioned that no traces of carbide phases were found in the milled Ti/C powder. This type of morphology seems to be very important to form a highly reactive titanium powder because the particle surface is protected from oxidation by the graphite matrix but is accessible for interaction with hydrogen because of the porous matrix microstructure. As can be estimated from Figure 4(A), the amount of surface and subsurface volume in titanium particles potentially acting as hydrogen sorption centers is in the Ti nanoparticles comparable to the remaining bulk of these particles. It was reported<sup>9</sup> that carbon acts as a reducing agent when added to Mg<sub>2</sub>Ni alloys. In that case this is quite plausible, since the heat of formation of NiO,  $H = -12$  kJ/g-atom,<sup>27</sup> is higher than that for CO<sub>2</sub>,  $H = -13$  kJ/g-atom,<sup>27</sup> and the latter is definitely stabilized by entropic contributions. In the case of TiO<sub>2</sub>, the heat of formation is  $H = -315$  kJ/g-atom,<sup>27</sup> which makes a reduction through

carbon highly improbable. The removal of the oxide shell from Ti particles seems in this case to be effectuated mainly by a mechanical process. The first two steps of the reaction of hydrogen with metallic elements are physisorption and chemisorption. Physisorption is enhanced by carbon, especially when it is nanoporous.<sup>28–30</sup> On the other hand, the dissociation of H<sub>2</sub> and subsequent chemisorption is greatly enhanced by metals, especially in the presence of *d*-electrons,<sup>31,32</sup> as is the case for Ti.

According to the binary Ti–H phase diagram,<sup>33</sup> the following order of phase transformations is carried out under equilibrium conditions:  $\alpha$ Ti  $\rightarrow$  solid solution of hydrogen in  $\alpha$ Ti  $\rightarrow$  (solid solution of hydrogen in  $\beta$ Ti)  $\rightarrow$   $\delta$ TiH<sub>2</sub>  $\rightarrow$   $\epsilon$ TiH<sub>2</sub>, where the solid solution of hydrogen in  $\beta$ Ti only forms at elevated temperatures above about 250 °C, wherefore it was set in brackets, and  $\epsilon$ TiH<sub>2</sub> is a tetragonally distorted modification of  $\delta$ TiH<sub>2</sub> at hydrogen contents above 2 H/Ti.<sup>33</sup> Additionally, a low-hydrogen-content metastable phase  $\gamma$ TiH<sub>0.01–0.03</sub> is reported.<sup>33</sup> In Ti/C powders, there are two distinct TPR peaks, with  $T_{\max} = 252$  °C and with  $T_{\max} = 423$  °C, with a weak third one at an intermediate temperature.  $\epsilon$ TiH<sub>2</sub> is present after the first TPR peak of milled Ti/C powders but has vanished after the second large TPR peak in the same sample, in favor of  $\delta$ TiH<sub>2</sub>, which under equilibrium conditions and in the absence of carbon, contains less H than  $\epsilon$ TiH<sub>2</sub>. This is a quite surprising result which needs further consideration.

The two-peak TPR curve observed for the Ti/graphite as-milled powder is the experimental evidence that in this case H atoms are located in two different types of occupation sites. Only C atoms introduced in titanium surface or subsurface layers can be the reason for these centers to appear. The C atoms are known to occupy octahedral positions<sup>33</sup> disturbing the neighbor tetrahedral positions suitable for H atoms. According to Blanter and co-workers<sup>22</sup> in the bcc  $\alpha$ Ti lattice, the C atoms affect significantly the behavior of H atoms with a strong attraction in the second shell (0.24 nm), whereas the first shell (0.18–0.2 nm) is blocked. The fact that no change in the lattice constants of Ti after the milling with graphite was observed (see Table 1) indicates that no Ti–C solid solution was formed during milling. This means that a segregation of C atoms can only have happened in near surface layers of the metal because of the close contact between graphite and metal at the surfaces. There are two evidences for this suggestion. The first evidence is the low-temperature reaction of H<sub>2</sub> with Ti resulting in the formation of about 25 wt % of  $\epsilon$ TiH<sub>2</sub> during the low-temperature reaction. A very localized near-surface segregation of C atoms changes the local site geometry for H atoms and the local Ti–H interaction activation energy, which is lowered by the attraction mentioned above. This makes the formation of  $\epsilon$ TiH<sub>2</sub> with a H-content  $\geq 2$  H/Ti probable in near-surface layers. With temperature rise during TPR, H can diffuse into the C-free bulk of the Ti powder particles where  $\delta$ TiH<sub>2</sub> is formed as is the case for Ti without C. The peak temperature is lower than in the absence of C, and this can be explained by diffusion enhanced by the modified surface layers. The formation of cubic  $\delta$ TiH<sub>2</sub> in nanoparticles most probably triggers the transformation of tetragonal  $\epsilon$ TiH<sub>2</sub> into the cubic phase. As was stated above,  $\epsilon$ TiH<sub>2</sub> is a tetragonally distorted modification of  $\delta$ TiH<sub>2</sub> at hydrogen contents above 2 H/Ti<sup>21</sup> so one can expect the transformation energy  $\delta$ TiH<sub>2</sub>  $\rightarrow$   $\epsilon$ TiH<sub>2</sub> to be quite small, probably smaller than the introduction of an energy consuming spherical phase boundary into the particles. The single peak TPD curve supports this suggestion.



After desorption of H, the pure Ti powders contain residual  $\alpha\text{Ti-H}$  solid solution as well as the metastable  $\gamma\text{TiH}_{0.01-0.03}$ , whereas in the Ti/C powders, two  $\alpha\text{Ti}$  solid solutions of H and/or C and the carbide  $\text{Ti}_2\text{C}$  can be detected. In both samples, the hydride phases are dissolved. Since TPD of Ti/C showed that not all of the H evolved from the sample but no hydride is left, the solid solutions in  $\alpha\text{Ti}$  must be one H solution and one C solution, the first being more probable in the larger metal particles, the latter in the small ones. The TiC found after TPD must have formed during desorption. From the point of view of thermodynamics, the formation of TiC is not surprising: the affinity of Ti to C is higher than H, as indicated by the heats of formation of TiC,  $H(298) = -92.26$  kJ/g-atom and  $\text{TiH}_2$ ,  $H(298) = -48.12$  kJ/g-atom.<sup>27</sup> So the reaction of Ti with C is more favorable than the reaction with H. On the other hand, the mobility of H is much higher than that of C. At the beginning of the sorption process, the hydrogen is in the gas phase and can form the hydride at low temperatures, a process which is enhanced by the near-surface layers modified by C, and only the hydrogen evolution during TPD promotes the precipitation of TiC. This phase significantly blocks the powder surface: hydrogen sorption falls down from  $1 \times 10^{22}$  molec  $\text{H}_2/\text{g Ti}$  to  $9 \times 10^{20}$  molec  $\text{H}_2/\text{g Ti}$  in the second TPR cycle. Thus, graphite modifies the near-surface layers of Ti in Ti/C powders, which drastically improves the reactivity of Ti toward  $\text{H}_2$ , until the surface is blocked by carbon-containing phases after TPD, so this reaction is suppressed.

The mechanical activation of structural and chemical transformations was also studied in the Zr–C–H system.<sup>34</sup> Here, Zr and C were milled in hydrogen flow. In the first stage, the formation of  $\text{ZrH}_2$  in a solid–gas reaction was observed, and in the second stage the formation of a Zr–C solid solution during decomposition of  $\text{ZrH}_2$  and formation of hydrocarbon was observed. In this system, which is chemically similar to the Ti–C–H system, it was found that the thermodynamically favorable carbide formation is initially suppressed for kinetic reasons but wins through after due time even in persistent hydrogen flow.<sup>34</sup> This result explains quite well why in the second TPR cycle of Ti/C powders, the hydrogen uptake is about 100 times less as compared to the first cycle.

## 5. Conclusions

It was shown that graphite added to Ti powder before mechanical activation significantly improves the reactivity of Ti toward  $\text{H}_2$ . We attribute these phenomena to several effects, as follows:

1. A stimulating effect of graphite on the powder-crushing process, which results in the formation of very fine Ti powder particles.
2. An anti-sticking and matrix-forming effect of graphite, which is exhibited in the formation of composite powder containing Ti nanoparticles randomly distributed in a porous graphite matrix.
3. A modifying effect of carbon atoms, which is exhibited in the modification of near-surface layers of Ti and leads to a drastic decrease in the effective activation energies of H uptake of Ti from 150 to 38–50 kJ/mol, and a drastic increase of H uptake from 0.5 H/Ti to 1.6 H/Ti. Unfortunately, upon desorption of hydrogen, the thermodynamically favorable carbide is

formed during the desorption of the hydride and suppresses the hydride formation in further loading–deloading cycles.

**Acknowledgment.** We are thankful to Dr. A. N. Streletskii (Institute of Chemical Physics PAS) for valuable comments and discussion, to Dr. H. Jander (Institute of Physical Chemistry of the University of Göttingen) for the preparation the TEM samples, and to A.B. Borunova (Institute of Chemical Physics PAS) for the specific surface area measurements. This work was partly supported by RFBR, project No 040332215.

## References and Notes

- (1) Schlappbach, L. *Solid State Commun.* **1981**, *38*, 117.
- (2) Zhang, H.; E. Kisi, H. *J. Phys.: Condens. Matter* **1997**, *9*, L 185.
- (3) Oelerich, W.; Klassen, T.; Bormann, R. *J. Alloys Compd.* **2001**, *32*, L5.
- (4) Dechouche, Z.; Klassen, T.; Oelerich, W.; Goyette, J.; T. Bose, K.; Schulz, R. *J. Alloys Compd.* **2002**, *347*, 319.
- (5) Sandrock, G.; Gross, K.; Thomas, G. *J. Alloys Compd.* **2002**, *339*, 199.
- (6) Janot, R.; Rougier, A.; Aymard, L.; Lenain, C.; Herrera-Urbina, R.; Nazri, G. A.; Tarascon, J. M. *J. Alloys Compd.* **2003**, *356–357*, 438.
- (7) Barkhordarian, G.; Klassen, T.; Bormann, R. *J. Alloys Compd.* **2004**, *364*, 262.
- (8) Dehouche, Z.; Goyette, J.; Bose, T. K.; Schulz, R. *Int. J. Hydrogen Energy* **2003**, *28*, 983.
- (9) Janot, R.; Aymard, L.; Rougier, A.; Nazri, G. A.; Tarascon, J. M. *J. Phys. Chem. Sol.* **2004**, *65*, 529.
- (10) Aymard, L.; Lenain, C.; Courvoisier, L.; Salver-Disma, F.; Tarascon, J. M. *J. Electrochem. Soc.* **1999**, *146*, 2015.
- (11) Imamura, H.; Takesue, Y.; Tabata, S.; Shigetomi, N.; Sakata, Y.; Tsuchiya, S. *Chem. Commun.* **1999**, 2277.
- (12) Bouaricha, S.; Dodelet, D.; Guay, D.; Huot, J.; Schulz, R. *J. Alloys Compd.* **2001**, *325*, 245.
- (13) Janot, R.; Aymard, L.; Rougier, A.; Nazri, G. A.; Tarascon, J. M. *J. Mater. Res.* **2003**, *18*, 1749.
- (14) Bobet, J. L.; Grigorova, E.; Khrussanova, M.; Khristov, M.; Stefanov, P.; Peshev, P.; Radev, D. *J. Alloys Compd.* **2004**, *366*, 298.
- (15) Mulana, F.; Nishiyama, N.; Matsumoto, A.; Tsutsumi, K. *J. Alloys Compd.* **2004**, *372*, 243.
- (16) Awasthi, K.; Kamalakaran, R.; Singh, A. K.; Srivastava, O. N. *Int. J. Hydrogen Energy* **2002**, *27*, 425.
- (17) Chen, Y.; Williams, J. S. *Mater. Sci. Forum* **1996**, *225/227*, 881.
- (18) Takasahi, A.; Kelton, K. F. *J. Alloys Compd.* **2002**, *347*, 295.
- (19) Mavrikakis, M.; Schwank, J. W.; Gland, J. L. *J. Chem. Phys.* **1996**, *105*, 8398.
- (20) Han, J. S.; Pezat, M.; Lee, J.-Y. *J. Less-Common Met.* **1987**, *130*, 395.
- (21) Fukai, Y. *The Metal–Hydrogen System Basic Bulk Properties*; Springer Series in Material Science, 21; Springer: Berlin, 1993.
- (22) Blanter, M. S.; Golovin, I. S.; Granovskiy, E. B.; Sinning, H.-R. *J. Alloys Compd.* **2002**, *345*, 1.
- (23) Maeland, A. J. In *Hydrogen in Disordered and Amorphous Alloys*; Bambakidis, G., Bowmann, R. C., Jr., Eds.; Plenum: New York, 1986.
- (24) Kirchheim, R. *Prog. Mat. Sci.* **1988**, *32*, 262.
- (25) Ron, M. *J. Alloys Compd.* **1999**, *283*, 178.
- (26) Borchers, C.; Leonov, A. V.; Khomenko, T. I.; Morozova, O. S. *J. Mater. Sci.* **2003**, *39*, 5259.
- (27) *Thermochemical Properties of Inorganic Substances*; Knacke, O., Kubaschewski, O., Hesselmann, K., Eds.; Springer: Berlin, 1991.
- (28) Nijkamp, M. G.; Raaymakers, J. E. M. J.; van Dillen, A. J.; de Jong, K. P. *Appl. Phys. A* **2001**, *72*, 619.
- (29) Chevallier, F.; Aymard, L.; Tarascon, J.-M. *J. Electrochem. Soc.* **2001**, *148*, A1216.
- (30) Texier-Mandoki, N.; Dentzer, J.; Piquero, T.; Saadallah, S.; David, P.; Vix-Guterl, C. *Carbon* **2004**, *42*, 2735.
- (31) Schlappbach, L.; Züttel, A.; Gröning, P.; Gröning, O.; Aebi, P. *Appl. Phys. A* **2001**, *72*, 245.
- (32) Schlappbach, L.; Züttel, A. *Nature* **2001**, *414*, 353.
- (33) San-Martin, A.; Manchester, F. D. *Bull. Alloy Phase Diagr.* **1987**, *8*, No 1, 30.
- (34) Borchers, C.; A. Leonov, V.; O. Morozova, S. *J. Phys. Chem. B* **2002**, *106*, 1843.